

Article

Optical Measurement of Planar Deformations in the Destructive Mechanical Testing of Masonry Specimens

Luís Filipe Lages Martins ^{1,*}, Ana Isabel Marques ², Álvaro Silva Ribeiro ¹, Paulo Candeias ³, Maria do Rosário Veiga ² and João Gomes Ferreira ⁴

¹ LNEC—National Laboratory for Civil Engineering, Scientific Instrumentation Centre, 1700-066 Lisboa, Portugal; asribeiro@lnec.pt

² LNEC—National Laboratory for Civil Engineering, Buildings Department, 1700-066 Lisboa, Portugal; aimarques@lnec.pt (A.I.M.); rveiga@lnec.pt (M.d.R.V.)

³ LNEC—National Laboratory for Civil Engineering, Structures Department, 1700-066 Lisboa, Portugal; pcandeias@lnec.pt

⁴ CERIS, IST, Ulisboa, 1649-004 Lisboa, Portugal; joao.gomes.ferreira@tecnico.ulisboa.pt

* Correspondence: lfmartins@lnec.pt; Tel.: +351-21-844-3000

Received: 13 December 2019; Accepted: 30 December 2019; Published: 3 January 2020



Featured Application: Planar deformation measurement in the destructive mechanical testing of masonry specimens, using an affine geometrical camera model.

Abstract: This paper addresses the planar measurement problem in the destructive mechanical testing of masonry specimens, describing the proposed optical measurement solution. The adopted affine geometrical camera model is described as well as its experimental implementation using a digital camera and a measurement referential traceable to the International System of Units (SI). Experimental results from non-destructive tests are presented and discussed, including measurements obtained from the use of classical contact instrumentation. Measurement estimates and uncertainties related to the quantified mechanical properties are also shown.

Keywords: destructive testing; masonry specimens; deformation; optical measurement

1. Introduction

This paper describes the optical methodology related to the planar deformation measurement problem in the destructive mechanical testing of masonry specimens, in the context of scientific research activities related to the study of the behavior of masonry walls in old buildings, built in the beginning of the 20th century, in the city of Lisbon (Portugal). Some of the old masonry buildings in the city of Lisbon have a high state of degradation and, as a consequence, a greater vulnerability to seismic actions. Despite all the scientific advances made in the context of the seismic vulnerability and structural reinforcement of these buildings, there is still a need for further research in this area, motivated by the minimization of the risk related to the loss of human lives.

Knowledge of the characteristics of resistant masonry walls is one of the aspects that still have gaps, mainly due to the difficulty in obtaining representative specimens. In addition, the growing interest in the rehabilitation of these buildings contributes to the search for new reinforcement solutions that are compatible with the original building construction techniques. It is equally important to ensure that these reinforcement techniques, in addition to the aesthetic and functional aspects, also reduce the seismic vulnerability of these buildings [1–3].

This research field is characterized by a reduced knowledge about the mechanical behavior of masonry walls and structural reinforcement techniques, compatible with those walls, aiming the improvement of the structural performance of this type of buildings, motivated by the high seismic risk in the Lisbon metropolitan area. In particular, the studied buildings include structural elements such as load-bearing masonry walls composed by solid and hollow ceramic bricks and bedding mortars composed by air lime. Therefore, a proper rehabilitation of this type of buildings can be compromised without a rigorous knowledge of the mechanical behavior of these elements, namely, the development of reinforcement techniques, which can contribute to increasing the structural safety of buildings.

Since masonry is a heterogeneous composite material on a mesoscopic level, essentially consisting of bricks and mortar joints, the analysis of its mechanical behavior is extremely complex [4]. The constituent elements themselves and the connection between them may be defective, which results in a nonlinear structural behavior when masonry is subjected to both static and dynamic loads. This behavior is usually accompanied by increasing anisotropy to increasing levels of deformation due to various physical phenomena that occur at different scales of observation, such as contact and friction between crack surfaces. These phenomena are directly related to the existence of defects present in the materials' microstructures [5]. However, masonry can also be analyzed from a macroscopic point of view on its overall behavior, which results from the combination of the constituent materials, in this case the behavior of ceramic bricks, bedding mortars, and the interaction between them.

The mechanical destructive testing of masonry specimens retrieved from the studied buildings, with nominal dimensions of 0.80 m (height), 0.70 m (length), and 0.25 m (width), gives a strong contribution to the knowledge improvement in this research field. However, in this type of dimensional testing, the use of conventional instrumentation, typically invasive methods such as measurement chains using LVDT (linear variable displacement transformer) sensors under dynamic conditions are known to have many constraints, namely because of risk of damage due to the destructive nature of the testing (namely, the fracture and collapse of the specimens).

The research and development of optical non-invasive systems and algorithms that provide novel solutions to obtain accurate measurements under dynamic and destructive conditions are being improved, and today these have a large potential to overcome the limitations of this type of conventional contact approach. The introduction of this new technique requires the validation of the process, considering the evaluation of measurement uncertainty and the traceability to SI.

This paper concerns the study of this measurement problem, including the development of a new non-invasive measurement solution based on non-contact optical measurement, in order to provide accurate and SI traceable planar deformation measurements in the tested masonry specimens.

Section 2 describes the classical instrumentation used in masonry specimen testing and presents the proposed alternative optical approach, namely, the measurement model, method, and system as well as the adopted digital image processing algorithm. The experimental work, based on non-destructive testing of masonry specimens, is described in Section 3, including the metrological characterization of the classical and the optical measurement chains used in this context, the description of the testing apparatus, and the obtained results. Section 4 describes the measurement uncertainty evaluation of the quantified mechanical quantities, which includes the instrumental measurement uncertainty related to the use of the classical and the optical measurement approach. A discussion of the obtained results is shown in Section 5.

2. Planar Deformation Measurement Methods in Masonry Specimens

2.1. Classical Instrumentation

The study of the structural behavior of masonry walls—composed by solid and hollow ceramic bricks and air lime bedding mortars—can be supported in multiple experimental activities, namely, mechanical testing in order to characterize this type of old building material when subjected to compressive or flexion actions. In general, testing machines and dedicated devices such as reaction

frames and hydraulic actuators are used in the assembly and testing of specimens representing the structural element in study. In addition to the force and displacement measurement chains that compose the testing equipment, the instrumentation of masonry specimens can include (see Figure 1):

- Unidimensional deformeters;
- Electrical strain gauges;
- LVDT sensors.

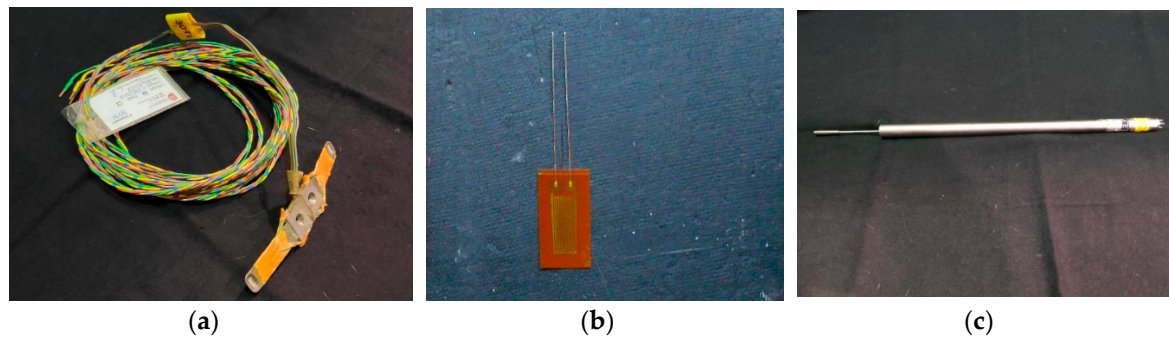


Figure 1. Classical instrumentation of masonry specimens: (a) unidimensional deformer; (b) electrical strain gauge; (c) linear variable displacement transformer (LVDT) sensor.

In general, these contact sensors are connected to a data acquisition system that provides electrical power and is responsible for the conditioning and processing of the electrical signals received. The existence of multiple measurement chains and the dynamic nature of the testing activities also imply the use of a synchronization signal generator. The collected data allows quantifying the relation between stress and the dimensional quantities (displacement or strain) in regions of interest in the tested specimen, namely in its central area, from which several mechanical properties can be obtained and used for its characterization, namely, the compressive strength, σ , the modulus of elasticity, E , and the Poisson ratio, ν , which are, respectively, determined by the following expressions:

$$\sigma = F_{\max}/A, \quad (1)$$

$$E = F_{\max}/(3 \times \varepsilon_v \times A), \quad (2)$$

$$\nu = \varepsilon_h/\varepsilon_v, \quad (3)$$

where F_{\max} is the maximum load force, A is the specimen's cross-section area (defined by the product between its length, l , and width, w), and ε_h and ε_v are the horizontal and vertical strains measured when the maximum stress is achieved. Both the horizontal and vertical strains are obtained from the ratio between the deformation, ΔL , observed between two points at the maximum stress and the initial length, L_0 , between the same two points before load application, i.e.,

$$\varepsilon = \Delta L/L_0 \quad (4)$$

$$\Delta L = L - L_0 \quad (5)$$

where L is the measured length between the two points at the maximum stress.

The overall calculation process related to the compressive mechanical testing of masonry specimens is shown in Figure 2.

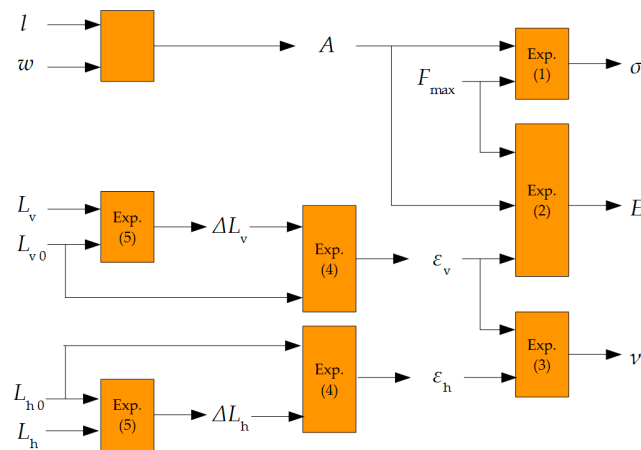


Figure 2. Functional diagram of the quantities and mathematical models related to the compressive mechanical testing of masonry specimens.

The determination of compressive strength requires the destructive testing of the specimen, which can seriously damage the above-mentioned sensors and, in the case of specimens with large dimensions retrieved from the old buildings, can significantly increase the economic cost of the performed testing activities, namely, when dealing with unique specimens with a high asset value. The loss of instrumentation during the collapse of the specimen also invalidates any measurement performed in that stage, thus not allowing any behavior analysis.

In the destructive compressive testing, LVDT sensors are usually placed on each frontal and rear surface of the specimen, aiming strain measurement in two directions (vertical and horizontal) for determination of the Poisson ratio. When the specimen begins to show the first signs of permanent deformation, the LDVT sensors are removed in order to avoid any damage, and the test progresses to the specimen collapse.

2.2. Proposed Optical Approach

2.2.1. Measurement Model and Method

The proposed optical measurement solution consists in the use of a single camera with a spatial position and orientation that allows the visualization of a set of targets distributed in a balanced way by different regions (in the static region surrounding the specimen and in the dynamic tested specimen surface). The use of a single camera instead of multiple cameras is justified by its simplicity, numerical stability, and less costly experimental apparatus, without compromising the intended measurement accuracy level.

In the geometrical modeling of the bi-dimensional image formation process in optical systems [6], it is possible to find two main categories of camera models—perspective and affine models—which can potentially be applied to the proposed optical measurement solution.

The perspective camera model (see Figure 3a) is usually applied in observation contexts that demand a highly rigorous geometrical accuracy, being related to complex and nonlinear mathematical formulation, for example, related to the lens distortion correction. The affine camera models are characterized by a higher simplicity, since they are approximations to the perspective model; therefore, they have a lower geometrical accuracy.

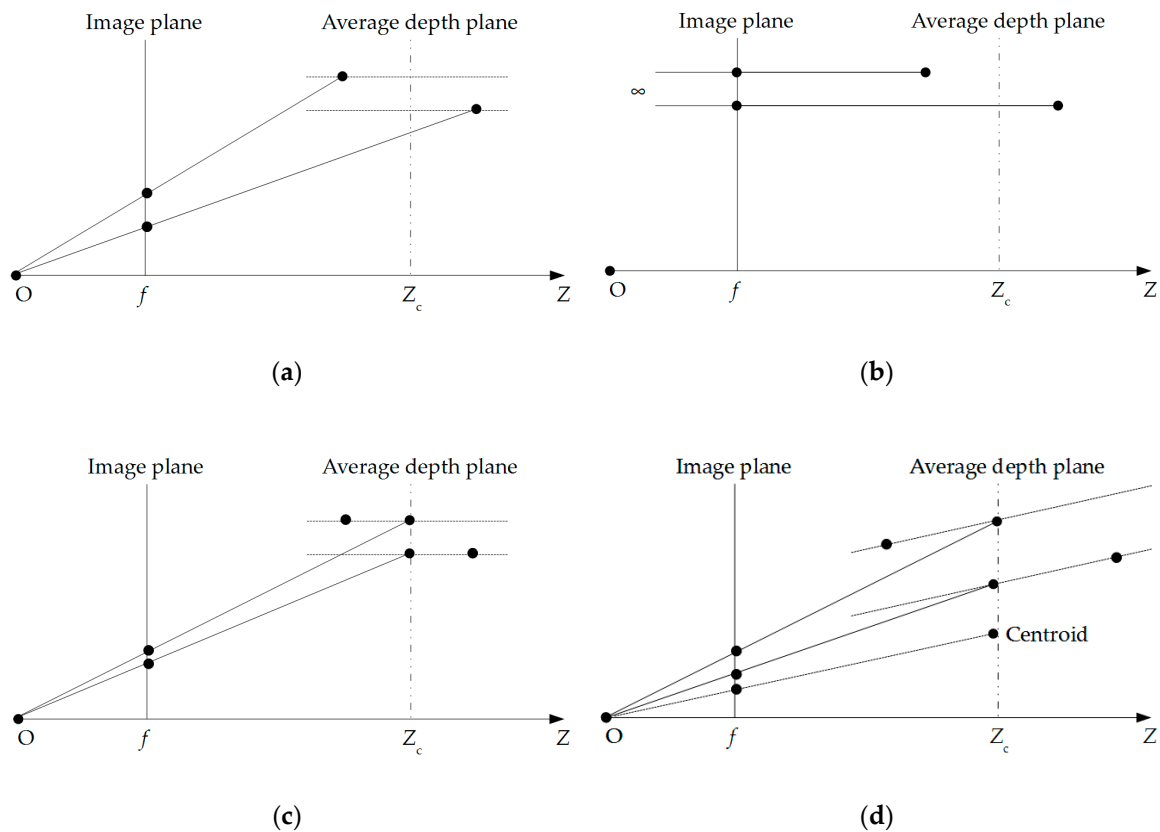


Figure 3. Geometrical camera models: (a) perspective; (b) orthographic; (c) weak perspective; (d) paraperspective (adapted from reference [6]).

Within the generalized affine camera models, it is possible to distinguish three particular cases: orthographic, weak perspective, and paraperspective.

The orthographic model (see Figure 3b) is the simplest affine camera model, where the depth of the three-dimensional component is ignored, and the optical center is located in infinity. This type of projection is also designated as parallel projection, since the projection lines established between points in space and in the image are parallel to each other and orthogonal to the image plane. It assumes a unitary scale coefficient and corresponds to an exact solution for camera modeling when using a telecentric lens (originates a constant magnification of objects seen in the field depth range, independent of the observation distance), or an approximate solution in the case of tele-objective lens (with a high focal length) and object visualization where the depth variation is quite reduced when compared with the observation distance).

The addition of a non-unitary uniform scale coefficient for both image axis to the orthographic model, relating the object dimension in the world (expressed in millimeters, for example) with the corresponding image dimension (usually expressed in pixels), originates the weak perspective model, as represented in Figure 3c. In this type of projection, object points are projected to the average depth plane, Z_c , parallel to the image plane, followed by a perspective projection with isotropic scaling to the image plane. For this reason, the weak perspective is also designated orthographic projection with uniform scaling, where a depth average value is used instead of the depth individual values of each object point (individual scaling), as it is of the case of the perspective projection. The projection error of the weak perspective model relative to the perspective model is minimized in the case of the use of a reduced focal length camera, narrow field-of-view, and reduced depth variation relative to the average depth plane.

In the paraperspective, as shown in Figure 3d, object points in space are projected to the average depth plane (parallel to the image plane) following a direction parallel to the line that passes through the object’s centroid and the camera optical center.

In this study, the weak perspective model or the orthographic model with uniform scaling, K , is adopted, allowing to relate the three-dimensional point position (X, Y, Z) in the world (expressed in millimeters, for example) with the corresponding bi-dimensional position (x, y) in the image (usually expressed in pixels), i.e.,

$$\Delta X = K \cdot \Delta x \tag{6}$$

$$\Delta Y = K \cdot \Delta y \tag{7}$$

where ΔX and ΔY represent the planar displacement of the point between two consecutive time observations, in the X (horizontal) and Y (vertical) directions, respectively, of the world coordinate system. In a similar way, Δx and Δy represent the corresponding planar point displacement in the x and y directions of the image coordinate system.

In the proposed approach, a measurement referential composed of reference targets is placed in front of the observation region in the masonry specimen (with length l and width w) at the minimum reasonable distance from the specimen surface in order to minimize the observation depth difference to the monitoring targets fixed and scattered in the observation region (in the inner region of the referential), as shown in Figure 4.

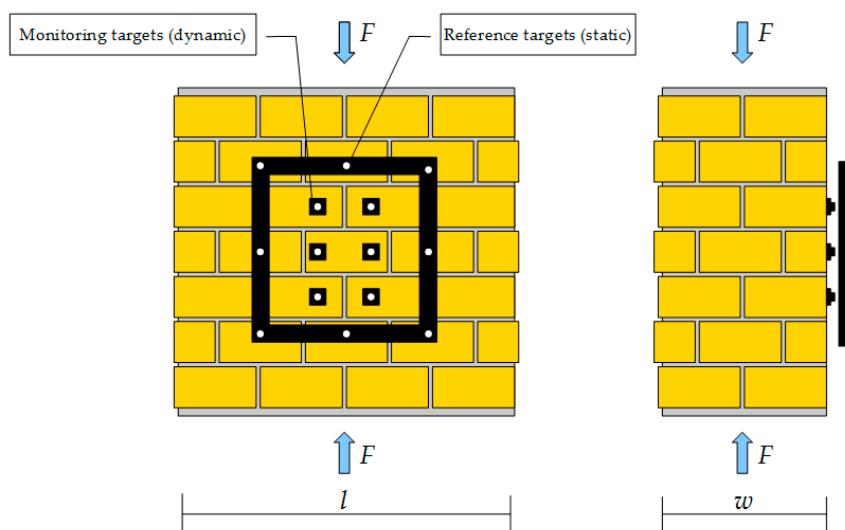


Figure 4. Schematic representation of the proposed optical measurement method.

As shown in Figure 4, the targets positioning on the specimen allows determining horizontal and vertical deformations, including bricks and mortar joints, making the deformation measurement representative of the overall deformation of the masonry specimen.

The mentioned referential is subjected, before the specimen testing, to dimensional measurement aiming at the determination of the three-dimensional world position of each reference target. The knowledge of these spatial coordinates supports the determination of the scale coefficient in each acquired image, since the measurement referential is placed in a static region of the specimen experimental setup (assuring that it does touch the specimen and is not subjected to vibrations produced by the testing machine). Through digital image processing, it is possible to obtain the corresponding two-dimensional image positions of the observed reference targets and calculate the scale coefficient between pairs of targets using the expression

$$K_{i,j} = D_{i,j}/d_{i,j} \tag{8}$$

where $i = j = 1, 2, \dots, n$, with $i \neq j$ and n being the total number of reference targets in the referential, and $D_{i,j}$ and $d_{i,j}$ are, respectively, the distances between the two targets i and j in the world and in the image coordinate system, i.e.,

$$D_{i,j} = \sqrt{[(X_i - X_j)^2 + (Y_i - Y_j)^2 + (Z_i - Z_j)^2]} \tag{9}$$

$$d_{i,j} = \sqrt{[(x_i - x_j)^2 + (y_i - y_j)^2]} \tag{10}$$

Since the measurement referential can have several pairs of reference targets, an average value of the scale coefficient and the correspondent standard deviation of the experimental sample can be obtained. This calculation procedure (represented in Figure 5) contributes to the reduction of the scale coefficient measurement uncertainty components related to the effect of the lens distortion and planar misalignments between the specimen surface, the measurement referential, and the image plane.

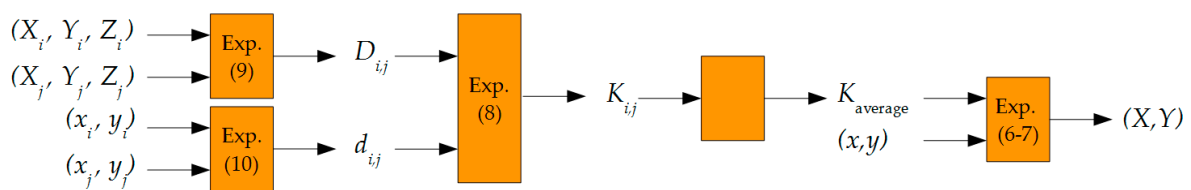


Figure 5. Functional diagram of the quantities and mathematical models related to the proposed optical approach.

It should be noticed that the reference target’s image coordinates can also be used to assess the referential static position stability and the turbulence effect on the optical path between the targets and the camera by analyzing low and high-frequency fluctuations in their position during testing.

2.2.2. Measurement System

The implemented optical measuring system for the masonry specimen testing setup is presented in Figure 6. In this figure, the main elements are numbered and described as follows:

1. Digital camera (brand Allied Vision Technologies, model Prosilica GX1050, Stadtroda, Germany), which includes the image sensor (CCD—charge-coupled device type, 1024 × 1024 pixels, 3.6 mm × 4.8 mm dimension, 5.5 μm squared pixel, acquisition frequency of 100 images per second, 14 bits radiometric resolution for gray-level images, exposure time between 10 μs and 26.8 s, GigE data communication and “mono8” image format), and an optical lens (with variable focal distance between 8 mm and 48 mm and C-type connection);
2. Telemetry device (brand Videotec, model DTMRX224, Schio, Italy) for remote adjustment of the camera’s focal distance, aperture, and lens focus, supported by a LabVIEW™ (National Instruments, Austin, Texas, USA) computational routine;
3. Signal generator (LNECs Scientific Instrumentation Centre, Lisbon, Portugal) for the synchronization of additional cameras and remaining instrumentation of the tested specimens (50% duty-cycle, frequency between 0.1 Hz and 114 Hz and variable frequency increments of 0.1 Hz and 1 Hz);
4. AVT Vimba computational application (version 1.3.0) for use with Allied Vision Technologies cameras, for image acquisition configuration, visualization, and image record purposes;
5. Measurement referential (LNEC’s Scientific Instrumentation Centre, Lisbon, Portugal), with eight reference targets (circular geometrical shape and 4 mm diameter, with known world coordinates), with a white color in order to have a high contrast relative to the remaining black surface of the referential;

6. Monitoring targets (LNEC’s Scientific Instrumentation Centre, Lisbon, Portugal), with unknown world coordinates, applied to the tested specimen, with the dimension and shape similar to the reference targets in the measurement referential.

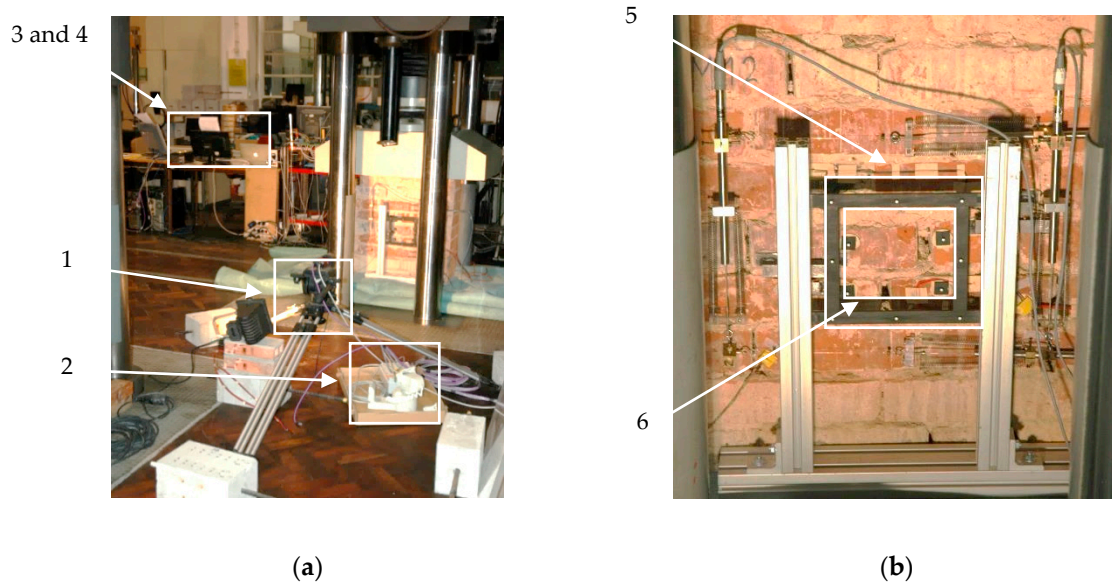


Figure 6. Experimental setup: (a) global view; (b) classical and optical measurement systems.

2.2.3. Digital Image Processing

The image digital processing was supported in a computational routine developed in MATLAB® (MathWorks, Natick, Massachusetts, USA), aiming at the determination of image coordinates of the geometrical center of both the reference and monitoring targets. In the case of the reference targets, the adopted target identification convention was a numerical sequence between one and eight, starting in the target located in the image upper left corner and following a clockwise direction for the following targets located in the measurement referential (see Figure 7a). For the case of the monitoring targets (located in the inner region of the measurement referential, as shown in Figure 7a), the mentioned numerical sequence was extended to these targets, continuing with the monitoring target located in the upper left corner of the referential inner region and following the clockwise direction for the remaining targets.

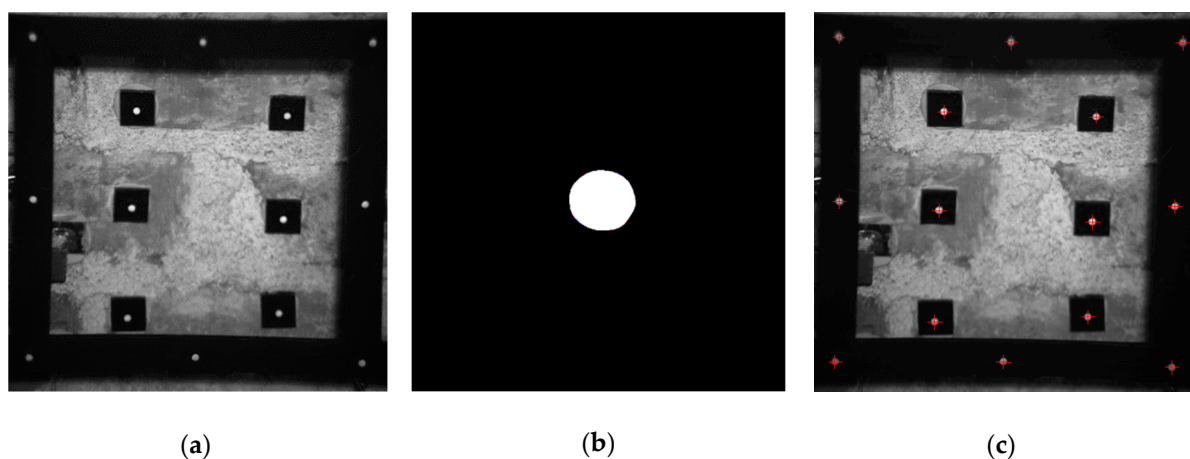


Figure 7. Target digital image processing: (a) original image; (b) binary image for one of the targets; (c) image with centroids.

The developed algorithm (schematically shown in Appendix A) is composed by the following sequential tasks:

1. Initialization (execution display configuration, memory, and command window cleaning, opened images closure and variable numerical format definition);
2. Assignment of numerical values to the input quantities:
 - a. Number of images;
 - b. Threshold (in gray level);
 - c. Window dimension (in pixels) around the targets, based on the lateral dimension of the target support and expected displacement;
 - d. Approximate image coordinates of the targets centroids (in pixels);
3. File opening for the record of target image coordinates;
4. Matrix initialization for the record of target image coordinates;
5. For each acquired image, execution of the following tasks:
 - a. Variable definition related to the original image designation;
 - b. Original image opening;
 - c. Matrix initialization with the targets individual sub-images;
 - d. Counter initialization related to the coordinates;
 - e. For each target visible on the image, execution of the following operations:
 - i. Definition of the interest area in the original image;
 - ii. Matrix initialization related to the target binary sub-image;
 - iii. Generation of the binary image by thresholding;
 - iv. Target identification;
 - v. Determination of the target centroid in the binary sub-image;
 - vi. Conversion of the target centroid image coordinates for the original image coordinate system;
 - vii. Record the target image coordinates;
 - f. Record the targets image coordinates in the output file;
 - g. Graphical representation of the centroids in the image (optional);
6. Closure of the targets image coordinates record file.

Figure 7 shows an example regarding three sub-images of a digitally processed target.

3. Experimental Testing

3.1. Metrological Characterization of the Optical Measurement Chain

Two identical measurement referentials (with designations A and B) were subjected to dimensional testing, aiming at the determination of the reference targets world coordinates, which are visualized in the camera's field-of-view.

These tests were performed in a laboratorial environment (controlled temperature between 19 and 21 °C, and relative humidity below 65%), using an SI traceable three-dimensional optical measuring machine (brand Mitutoyo, model QV APEX 302 PRO, Kawasaki, Kanagawa, Japan), with a measurement interval of 300 mm × 200 mm × 200 mm, resolution equal to 0.1 μm and an instrumental measurement accuracy of 5 μm, as the reference equipment.

Figure 8 shows the dimensional measurement of referential A in the mentioned optical measuring machine. Tables 1 and 2 show the estimates and sample experimental standard deviations of the

reference targets' world coordinates for the measurement referentials A and B, respectively, considering the targets' identification and the coordinate system shown in Figure 8.

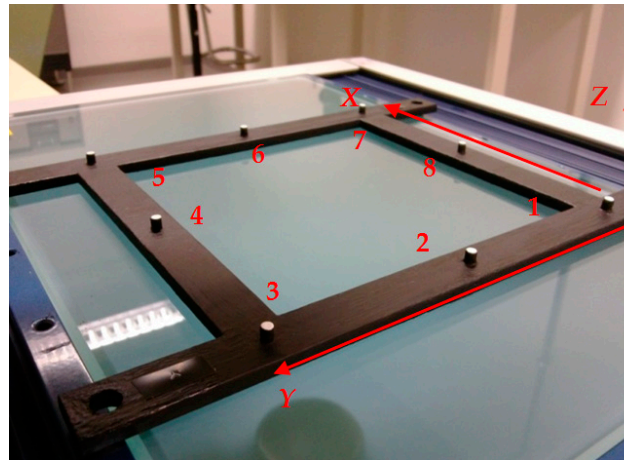


Figure 8. Dimensional measurement of the reference targets in the optical measuring machine.

Table 1. Three-dimensional spatial coordinates of the reference targets—referential A.

Target Identification	X /mm	Y /mm	Z /mm
1	10.320 ± 0.009	10.153 ± 0.030	5.105 ± 0.031
2	10.344 ± 0.010	100.137 ± 0.033	5.023 ± 0.011
3	10.387 ± 0.019	189.870 ± 0.033	5.070 ± 0.024
4	100.241 ± 0.018	189.803 ± 0.026	5.152 ± 0.017
5	190.090 ± 0.016	189.852 ± 0.032	5.266 ± 0.039
6	189.827 ± 0.009	99.927 ± 0.031	4.939 ± 0.012
7	190.081 ± 0.012	9.926 ± 0.029	4.973 ± 0.010
8	100.318 ± 0.012	10.047 ± 0.030	4.934 ± 0.006

Table 2. Three-dimensional spatial coordinates of the reference targets—referential B.

Target Identification	X /mm	Y /mm	Z /mm
1	10.197 ± 0.018	10.733 ± 0.034	5.077 ± 0.028
2	10.183 ± 0.032	100.785 ± 0.036	4.936 ± 0.015
3	10.213 ± 0.057	190.752 ± 0.032	4.959 ± 0.011
4	100.437 ± 0.054	190.655 ± 0.016	4.858 ± 0.007
5	190.448 ± 0.053	190.558 ± 0.025	4.811 ± 0.012
6	190.007 ± 0.035	100.710 ± 0.026	4.928 ± 0.011
7	190.112 ± 0.022	10.751 ± 0.025	5.032 ± 0.037
8	100.135 ± 0.024	10.920 ± 0.017	5.198 ± 0.009

The measurement samples of the reference targets show a dispersion of values comprised between 9 and 57 μm, which can be considered as a major measurement uncertainty component, reflecting the influence of shape deviation of each target in the measurement of the center three-dimensional coordinates. Estimates of the Z coordinate show a variation of 0.1 mm order of magnitude close to the nominal value of 5 mm, which is considered suitable for the adopted camera model (weak perspective) and implemented observation distance.

3.2. Metrological Characterization of the Contact Measurement Chain

Although not used in the destructive compressive testing of masonry specimens, this study included the metrological characterization of contact dimensional measurement chains with LVDT

sensors in order to establish a comparative basis relative to the proposed alternative measurement approach described in Section 2.2. In a first stage, this laboratorial task included the horizontal calibration of the LVDT sensors (composed by its fixed coil housing and the moveable core stem) without assembly accessories (springs) and, in a second stage, the vertical calibration with and without the assembly accessories. This last stage aimed to determine the magnitude of the measurement uncertainty component related to the LVDT installation onto the masonry specimen to be tested, namely, the impact of the measurement position and the use of springs.

The tested LVDT sensors (brand HBM, model W50K, Darmstadt, Germany), with a measurement interval between ± 50 mm, were calibrated in a controlled laboratorial environment (temperature between 19 and 21 °C, and relative humidity below 65%), based on the electrical tension readings obtained through the data acquisition system (brand HBM, model Spider 8, Darmstadt, Germany) to which each LVDT sensor was connected. In the horizontal calibration, displacement reference values were obtained from SI traceable measurement standard equipment, a unidimensional measuring machine (brand Trimos, model Tulum 0210-450, Renens, Switzerland), with a 200 mm range, resolution equal to 0.1 μm and instrumental measurement accuracy of 1 μm . From the sample of eight LVDT sensors calibrated in the horizontal position, the following maximum values of standard uncertainties were obtained: (i) calibration, 1.3 μm ; (ii) repeatability, 3.0 μm ; (iii) linearity, 36 μm .

In the second stage, the LVDT sensors were assembled in a vertical column having an SI traceable measurement standard displacement calibrator (brand Sylvac, model P50, Yverdon-les-Bains, Switzerland), with a 50 mm range, resolution equal to 0.1 μm , and with an instrumental measurement accuracy of 1 μm . Reference displacement values and the corresponding LVDT sensor readings in the data acquisition system were obtained. Tests were performed with and without the complete set of assembly accessories (including two springs). Although a similar calibration standard uncertainty was obtained, significant changes were observed in (i) repeatability, which increased up to 47 μm (with accessories) and up to 43 μm (without accessories), and (ii) linearity, which increased up to 115 μm .

These differences (relative to the horizontal position) are justified by (i) the vertical misalignment between the LVDT core stem and the measurement standard vertical axis, (ii) the type of stem (non-telescopic, with free movement), and (iii) the transverse movement of the core stem inside the coil housing, which does not occur in the horizontal position, where the core stem follows the inner surface of the coil housing by the gravity effect.

These results illustrate the measurement accuracy vulnerability in the use of LVDT sensors for displacement measurements. The proposed optical approach, as described in Section 2.2, is a non-contact measurement that can not only be used in destructive testing but, in addition, it is less vulnerable to measurement uncertainty components related to instrumentation assembly onto the masonry specimen.

3.3. Experimental Apparatus

Solid and hollow ceramic brick masonry specimens were retrieved from the walls of one building built in the beginning of the 20th century in the city of Lisbon (Portugal), which was undergoing rehabilitation.

These specimens were prepared and instrumented for testing at LNEC, with the classical apparatus described in Section 2.1. In particular, eight LDVT sensors were installed in the central region of the specimen frontal and rear surfaces (see Figure 6b), four of them in a vertical position (aiming the determination of the modulus of elasticity based on the measured vertical force and corresponding deformation), and the remaining four in a horizontal position, in order to determine the horizontal strain, and consequently, the Poisson ratio. All the LVDT sensors were fixed directly onto the specimen's ceramic bricks, avoiding bedding joints.

The proposed optical approach was also implemented by fixing monitoring targets in the specimen's ceramic bricks and placing the measurement referential with the reference targets close to the observation surfaces (see Figure 6b). The observation distance of the camera relative to the

specimen observation surface was optimized in order to establish a suitable field-of-view (with all the monitoring and reference targets visible on the image) and the maximum spatial resolution on the recorded images.

Readings from the LVDT sensors and camera images were properly synchronized using a dedicated signal generator, as schematically shown in Figure 9.

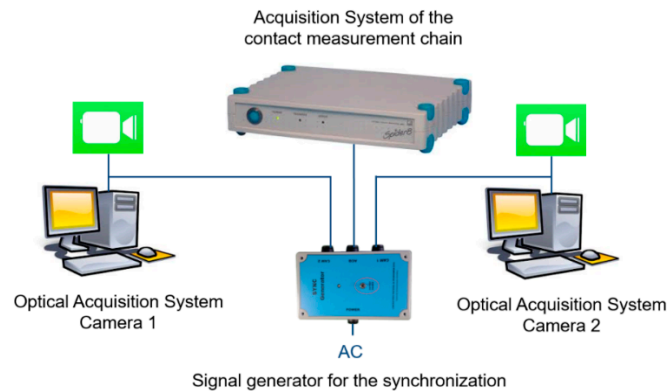


Figure 9. Synchronization of image acquisition and contact measurements.

The specimens were subjected to axial compression in a universal testing machine (brand SERVOSIS MFL, model UPS 5000 V, Madrid, Spain) NP 4015-1:1990 force class 0.5 in the measurement interval comprised between 300 and 3000 kN, as shown in Figure 6a, based on an adaptation of the standardized method described in EN 1052-1:1998 [7]. Since the specimens' fracture stress is unknown, several increasing loading and unloading cycles were carried out for both solid ceramic brick masonry specimens (increments of 100 kN, starting from 100 kN) and hollow ceramic brick masonry specimens (increments of 50 kN, starting at 50 kN, due to the known reduced axial compression resistance when compared with solid brick masonry). A total of three cycles were performed for each load level, considering loading speeds between 0.5 and 1.5 kN·s⁻¹ (as the maximum applied compression force increased throughout the performed cycles, the loading speed was also increased [8–10]). For safeguard purposes, LVDT sensors were removed after the appearance of cracks in the bricks, since the collapse of masonry specimens is quite fragile and destructive, as shown in Figure 10.



Figure 10. Collapse mechanism resulting from compression tests: (a) ceramic hollow brick specimen; (b) ceramic solid brick specimen.

3.4. Results

A first step in the application of the proposed optical measurement approach is the determination of the scale coefficient for each performed mechanical test, based on the previous laboratorial results of the metrological characterization of the used measurement referential (shown in Tables 1 and 2) and in the corresponding reference targets image coordinates. Tables 3 and 4 show an example of the obtained input quantities estimates, respectively, for referentials A and B.

Table 3. Reference targets image and world coordinates—referential A.

Target Identification	<i>x</i> /pixel	<i>y</i> /pixel	<i>X</i> /mm	<i>Y</i> /mm	<i>Z</i> /mm
1	92.7	24.6	10.032	10.153	5.105
2	72.5	502.7	10.344	100.137	5.023
3	37.1	977.6	10.387	189.870	5.070
4	492.7	972.9	100.241	189.803	5.152
5	933.2	983.0	190.090	189.852	5.266
6	955.3	531.8	189.827	99.927	4.939
7	996.0	57.7	190.081	9.926	4.973
8	551.5	48.3	100.318	10.047	4.934

Table 4. Reference targets image and world coordinates—referential B.

Target Identification	<i>x</i> /pixel	<i>y</i> /pixel	<i>X</i> /mm	<i>Y</i> /mm	<i>Z</i> /mm
1	85.8	72.1	10.197	10.733	5.077
2	533.8	96.8	10.183	100.785	4.936
3	984.8	110.9	10.213	190.752	4.959
4	957.4	547.4	100.437	190.655	4.858
5	942.7	978.5	190.448	190.558	4.811
6	498.9	948.5	190.007	100.710	4.928
7	57.1	934.4	190.112	10.751	5.032
8	77.9	505.6	100.135	10.920	5.198

These estimates can be applied to Equations (8)–(10) in order to obtain the corresponding scale coefficient measurement samples with a dimension equal to 28 (see Tables A1 and A2 in Appendix B). In the presented calculation example, an average value of 0.19650 mm·pixel^{−1} was obtained for images where the referential A is visible, and an average value of 0.20559 mm·pixel^{−1} was obtained for the case of referential B. Figure 11 illustrates the dispersion of scale coefficient values obtained for both measurement referentials (A and B).

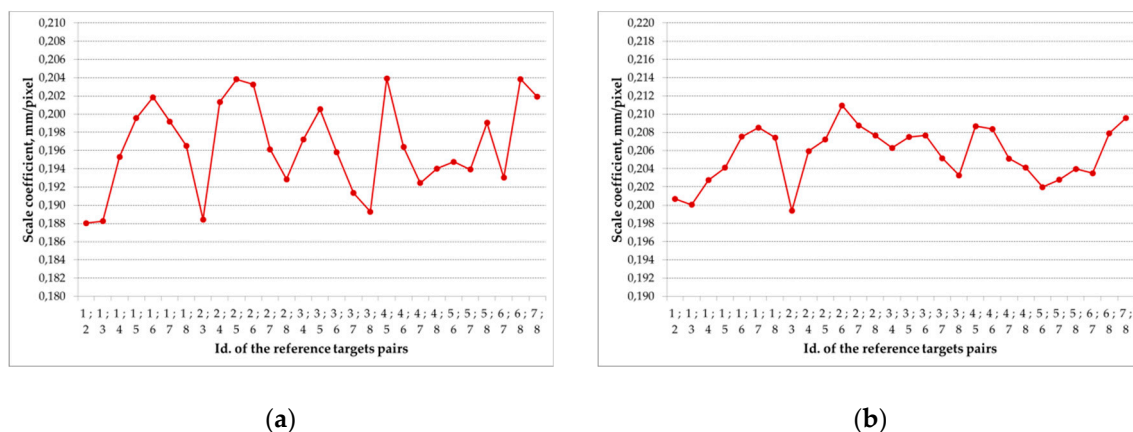


Figure 11. Dispersion of the scale coefficient values for: (a) referential A; (b) referential B.

In addition to the axial compression force reading obtained from the used universal testing machine, vertical and horizontal dimensional measurements were performed in the frontal and rear surfaces of the specimen, as shown in Figure 12, noticing that the contact and the optical measurement points are not spatially coincident.

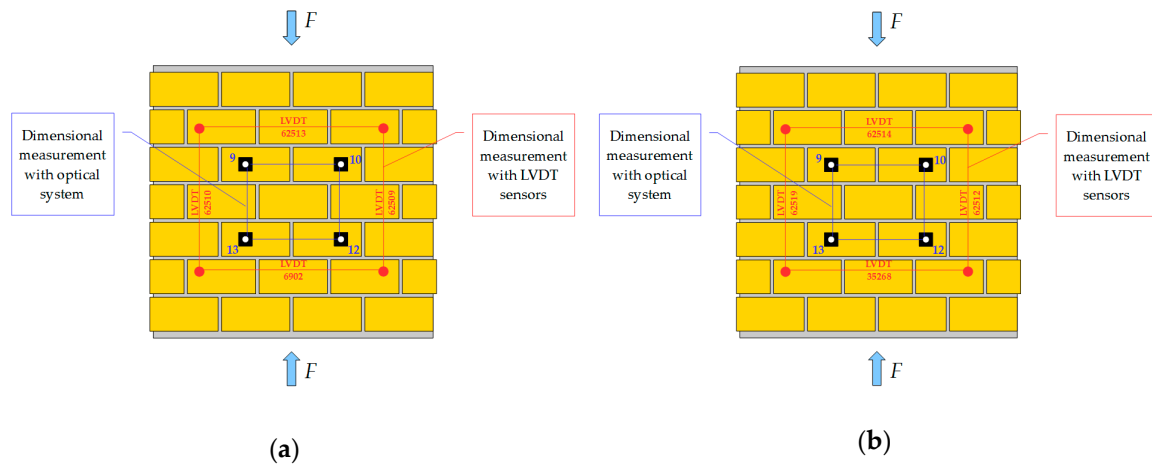


Figure 12. Measurement points in the specimen’s (a) frontal surface; (b) rear surface.

Based on the specimen’s length and width measurements (exemplified in Appendix C, Table A4), stress versus strain curves, regarding the loading and unloading cycle corresponding to 1/3 of the fracture stress, were obtained as shown in Figure 13 for the case of a solid brick specimen (ID M0M10). Figure 13a presents the values based in the contact dimensional measurement chain and Figure 13b presents the values based in the optical measuring system, referring to the same observation surface and illustrating the determination of the modulus of elasticity.

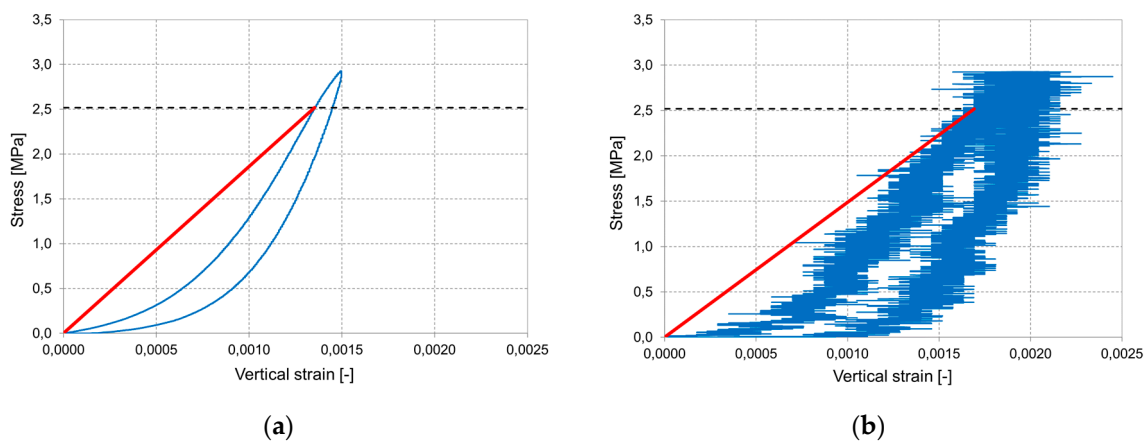


Figure 13. Stress versus strain curve for the masonry specimen, id M0M10, obtained by (a) contact dimensional measurements; (b) optical dimensional measurements.

Figure 13b shows the presence of noise in the extension measurements obtained by the optical dimensional measurements, when compared with the strain measurements obtained by the contact measurement chain (Figure 13a). This is justified by the low spatial resolution of the acquired images, which affects the targets image coordinates that support the deformation measurement. A higher spatial resolution can be achieved with an image sensor composed by smaller pixels or by using a different lens that is capable of producing a higher image magnification with an acceptable narrow field-of-view.

From the collected data, the main compressive mechanical properties of the tested masonry specimens were calculated using Equations (1)–(3), namely, the compressive strength, the modulus of elasticity, and the Poisson ratio, which were obtained from both the contact and the optical dimensional

measurement chains. An example of these measurement estimates is presented in Table 5 for a set of hollow and solid masonry specimens.

Table 5. Mechanical properties estimates of some tested masonry specimens.

Specimen Identification	Specimen Type	Compressive Strength /MPa	Contact Measurement Chain		Optical Measurement Chain	
			Modulus of Elasticity /GPa	Poisson Ratio	Modulus of Elasticity /GPa	Poisson Ratio
M0F3	Hollow	2.053	1.32	0.31	1.47	0.32
M0F7		2.272	0.96	0.06	0.73	0.07
M0F9		2.194	1.99	0.05	0.52	0.08
Average value		2.173	1.42	0.14	0.91	0.16
Average std. deviation		0.064	0.30	0.09	0.29	0.08
M0M9	Solid	5.338	2.12	0.10	1.71	0.17
M0M10		7.515	1.87	0.06	1.50	0.36
M0M12		4.194	3.20	0.17	1.75	0.07
Average value		5.682	2.40	0.11	1.65	0.20
Average std. deviation		0.974	0.41	0.03	0.08	0.09

Regarding the comparison of the main results, which generally provide a good agreement between the Poisson ratio and some discrepancy of values relates with the measurement of the modulus of elasticity, the differences found could be explained by the nature of the methods applied. In fact, considering that the testing is developed under dynamic conditions, the mechanical contact between the LVDT sensors and the specimen influences the estimates of measurement and its uncertainty. A better understanding of the impact of this source of error should be further studied in order to consider other types of specimens together with a sensitive analysis of the quantities that contribute to the uncertainty budget. Other possible sources of measurement uncertainty, namely, the time delay on acquisition and resolution, were disregarded.

With respect to the compressive strength, the measurement sample shows that the solid specimens are characterized by higher estimates, as expected for this type of masonry, in addition to a higher dispersion of values, when compared with the hollow specimens. Independently of the used measurement system, the modulus of elasticity related to the solid specimens is also higher when compared to the hollow specimens. In terms of the Poisson ratio, similar estimates and experimental dispersion of values are obtained, considering both types of test masonry specimens.

Comparisons between estimates and dispersion of values related to different measurement systems are not recommended at this stage, since the instrumental measurement uncertainty related to each dimensional measurement system is only presented in Section 4, in addition to the fact that we are dealing with different points of measurement and a complex spatial mechanical behavior of the specimens.

4. Measurement Uncertainty Evaluation

4.1. Calculation of the Output Measurement Uncertainties

As mentioned before, three main output quantities are usually defined in the context of the determination of the compressive mechanical testing of masonry specimens: the compressive strength, the modulus of elasticity, and the Poisson ratio defined, respectively, by Equations (1)–(3). The application of the uncertainty propagation law [11] to these mathematical models allows obtaining expressions for the corresponding measurement uncertainties

$$u(\sigma) = [(1/A^2) \cdot u^2(F_{\max}) + (F_{\max}^2/A^4) \cdot u^2(A)]^{0.5} \quad (11)$$

$$u(E) = \{[1/(9 \cdot \varepsilon_v^2 \cdot A^2)] \cdot u^2(F_{\max}) + [F_{\max}^2/(9 \cdot \varepsilon_v^4 \cdot A^2)] \cdot u^2(\varepsilon_v) + [F_{\max}^2/(9 \cdot \varepsilon_v^2 \cdot A^4)] \cdot u^2(A)\}^{0.5} \quad (12)$$

$$u(\nu) = \{(1/\varepsilon_v^2) \cdot u^2(\varepsilon_h) + (\varepsilon_h^2/\varepsilon_v^4) \cdot u^2(\varepsilon_v)\}^{0.5} \quad (13)$$

where $u(A)$ is given by

$$u^2(A) = w^2 \cdot u^2(l) + l^2 \cdot u^2(w). \tag{14}$$

The measurement uncertainty of the vertical or horizontal strain, ε , is given by

$$u(\varepsilon) = [(1/L_0^2) \cdot u^2(\Delta L) + (\Delta L^2/L_0^4) \cdot u^2(L_0)]^{0.5}. \tag{15}$$

This expression can be simplified based on the ΔL definition given by Expression (5) and on the assumption that $u(L) = u(L_0)$, originating the following expression for the strain measurement uncertainty

$$u(\varepsilon) = [(2 + \Delta L^2/L_0^2) \cdot (1/L_0^2) \cdot u^2(L)]^{0.5}, \tag{16}$$

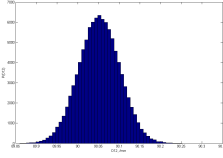
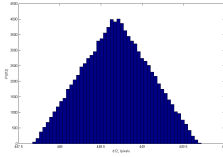
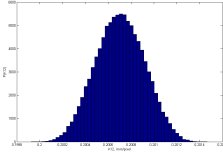
which is related to each dimensional method (optical or contact).

Appendix C lists the measurement uncertainty calculations related to the specimen’s cross-section area and maximum load force, while the following Sections 4.2 and 4.3 describe, in detail, the determination of the strain measurement uncertainty, respectively, for the optical and the contact method.

4.2. Measurement Uncertainty for the Optical Method

Due to the nonlinear models (Equations (9) and (10)) applied in the determination of the individual scale coefficients, the Monte Carlo method (MCM) [12] was used in the evaluation of the corresponding measurement uncertainties. Estimates of the reference targets image and world coordinates, as exemplified in Tables 3 and 4, were used in the performed simulations assuming uniform probability density functions (PDF) for the image coordinates with a semi-amplitude of 0.25 pixels, and a Gaussian PDF was used for the world coordinates with standard uncertainties equal to the obtained sample experimental standard deviations (see Tables 1 and 2). Table 6 exemplifies the results obtained for the intermediate and output quantities (in this case for the individual scale coefficient calculated with targets 1 and 2 of referential B), based on 10^5 trials.

Table 6. Results of the MCM simulation for the determination of the measurement uncertainty of scale coefficient $K_{1,2}$ obtained with referential B. PDF: probability density functions.

Quantity	Estimate	95% Expanded Uncertainty	Computational Accuracy	Numerical PDF
$D_{1,2}$	90.52 mm	0.097 mm	<0.002 mm	
$d_{1,2}$	448.68 pixels	0.78 pixel	<0.01 pixel	
$K_{1,2}$	0.200 70 mm·pixel ⁻¹	0.000 41 mm·pixel ⁻¹	<1 × 10 ⁻⁵ mm·pixel ⁻¹	

Although a triangular PDF was obtained for the $d_{1,2}$ intermediate quantity, the scale coefficient PDF showed a geometrical shape close to a Gaussian PDF. Suitable computational accuracy levels were obtained in the performed numerical simulations.

The application of the uncertainty propagation law to expressions (6,7) allows determining the standard measurement uncertainty related to the dimensional optical measurement, given by

$$u(L) = u(X) = u(Y) = [l^2 \cdot u^2(K_{\text{average}}) + K_{\text{average}}^2 \cdot u^2(l)]^{0.5} \tag{17}$$

where the standard uncertainty of the targets' image coordinates is majorated by a spatial resolution equal to 0.25 pixel, considering a uniform PDF, i.e.,

$$u(l) = u(x) = u(y) = 0.25 \text{ pixel}/\sqrt{3} = 0.07 \text{ pixel}. \tag{18}$$

The standard uncertainty of the average scale coefficient corresponds to

$$u(K_{\text{average}}) = [u_{\text{max}}^2(K_i) + s^2(K_i)/n]^{0.5} \tag{19}$$

where $s(K_i)$ is the experimental standard deviation of the scale coefficient measurement sample with dimension n (equal to 28, see Tables A1 and A2 in Appendix B). This measurement uncertainty is majorated by the use of the maximum measurement uncertainty, $u_{\text{max}}(K_i)$, which was obtained in the complete set of individual scale coefficients.

Table 7 shows the obtained estimates and standard uncertainties of the average scale coefficients for both referentials A and B.

Table 7. Cross-section area measurements in tested masonry specimens.

Referential	Estimate /mm·pixel ⁻¹	Standard Uncertainty /mm·pixel ⁻¹
A	0.196 50	0.000 97
B	0.205 59	0.000 63

These results were used in the determination of the standard measurement uncertainty related to the dimensional optical measurement (by use of Equation (17)), being posteriorly used to calculate the strain standard uncertainty (Equation (16)) and, in a last stage, the modulus of elasticity and the Poisson ratio. Figure 14 shows the measurement estimates and standard uncertainties obtained for the tested masonry specimens, taking into account the specimen's cross-section area and maximum load force measurement uncertainties described in Appendix C.

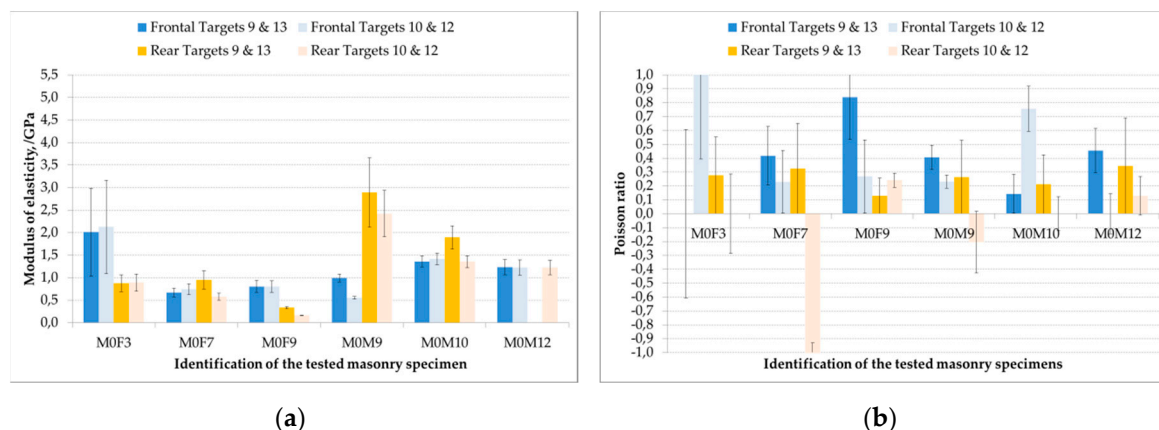


Figure 14. Estimates and standard uncertainties obtained from the optical measurement system for (a) the modulus of elasticity; (b) and the Poisson ratio.

With respect to the modulus of elasticity, a standard uncertainty between 0.07 and 0.60 GPa was obtained considering a measurement sample with dimensions equal to four (two measurements on the

frontal and rear observation surfaces). Significant differences were obtained between the frontal and rear measurements, namely, for specimens with ID M0F3 (hollow) and ID M0M9 (solid), justified by a spatial complex mechanical behavior of the tested specimens.

The results related to the Poisson ratio show a standard uncertainty between 0.19 and 0.51, making this measurement quite inaccurate, when compared with the expected dimension of the measurement interval for this type of material. This is justified by the higher relative measurement uncertainty of the horizontal strain (reduced deformations, close to 0.01 mm and near the spatial resolution of the acquired images) when compared with the vertical strain characterized by higher deformations. Again, the spatial complex mechanical behavior of the tested specimens is seen in the Poisson ratios, namely, in the case of opposite algebraic sign within the same masonry specimen.

4.3. Measurement Uncertainty for the Contact Method

The metrological characterization described in Section 3.2 supported the determination of the standard measurement uncertainty related to the contact dimensional measurement which was posteriorly used to calculate the strain standard uncertainty (by the application of Equation (16)) and, in a last stage, the modulus of elasticity and the Poisson ratio. Figure 15 shows the measurement estimates and standard uncertainties obtained for the tested masonry specimens, taking into account the specimen’s cross-section area and maximum load force measurement uncertainties described in Appendix C.

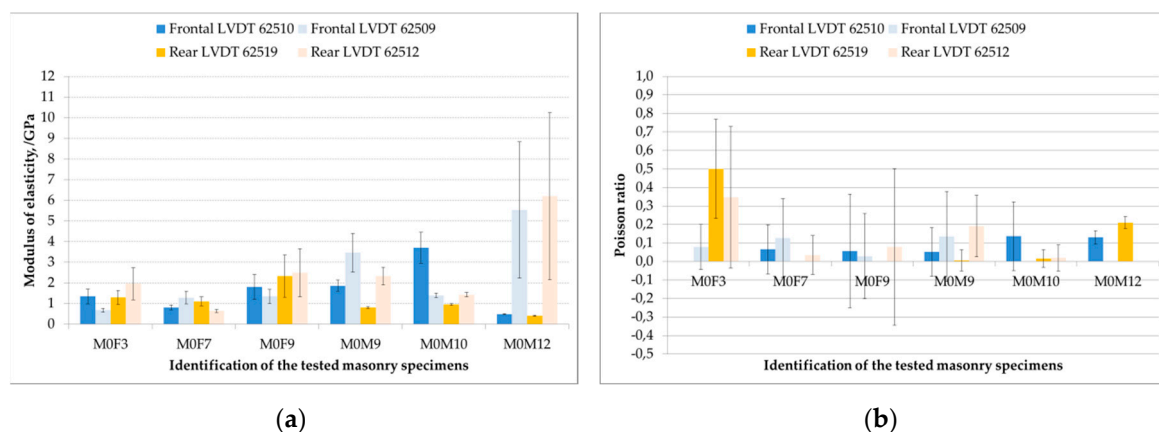


Figure 15. Estimates and standard uncertainties obtained from the contact measurement system for (a) the modulus of elasticity; (b) and the Poisson ratio.

A standard uncertainty comprised between 0.18 and 0.78 GPa was obtained for the modulus of elasticity, excluding a 1.9 GPa dispersion value obtained for the specimen with ID M0M12. In this specimen, significant differences were obtained between strain measurements in the frontal and the rear specimen surfaces.

The results related to the Poisson ratio show a standard uncertainty between 0.10 and 0.32, making this measurement quite inaccurate, since this variation has a similar dimension to the expected measurement interval.

4.4. Comparison between the Optical and the Contact Measurement Methods

This section aims the comparison between the modulus of elasticity and Poisson ratio measurements obtained from both the optical and the contact measurement methods, considering average values obtained from the four local measurements performed in each specimen. Figure 16 shows the corresponding estimates and measurement uncertainties for the modulus of elasticity and Poisson ratio.

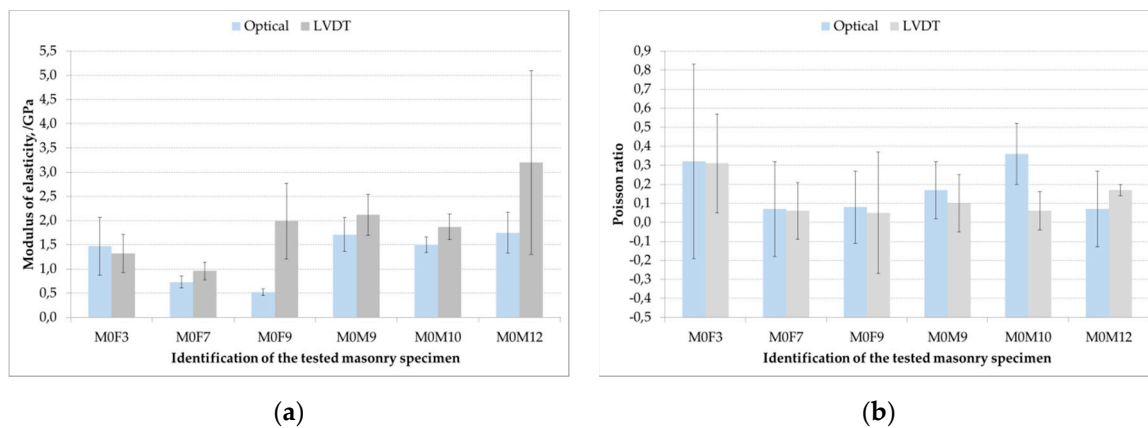


Figure 16. Estimates and standard uncertainties obtained from the optical and the contact measurement systems for (a) the modulus of elasticity; (b) and the Poisson ratio.

Concerning the modulus of elasticity, the contact measurement method provided estimates with a higher magnitude, namely, in the case of specimen ID M0M12. In general, the dispersion of values related to each measurement method overlap, with the exception of the specimen IDs M0MF9 and M0M12.

With respect to the Poisson ratio, the optical method provided slightly higher estimates in the majority of the tested specimens, noticing an overlap of the dispersion of values in most cases with a high magnitude.

5. Discussion

The performed study allowed identifying the strain measurement as the major component of instrumental measurement uncertainty related to the modulus of elasticity and the Poisson ratio for both methods. In the case of the optical method, this uncertainty component reflects the influence of the spatial resolution of the acquired images and the dispersion of the scale coefficient related to the effect of the lens distortion and planar misalignments between the specimen surface, the measurement referential, and the image plane. In the case of the contact method, the LVDT sensor repeatability and linearity have a strong impact on the dimensional measurement uncertainty and are mainly due to its assembly onto the masonry specimen and the use of installation accessories.

Regarding the modulus of elasticity, the instrumental measurement uncertainty related to the optical approach (between 0.07 and 0.60 GPa, as mentioned in Section 4.2) has a slightly reduced magnitude when compared with the instrumental measurement uncertainty of the contact measurement method (between 0.18 and 0.78 GPa). In both cases, the dispersion of values related to the modulus of elasticity is higher than the measurement sample dispersion, between 0.08 and 0.30 GPa, as shown in Table 5.

Regarding the Poisson ratio, both measurement methods show high values of measurement uncertainty, namely, the optical method due to the reduced spatial resolution affecting the measurement of the horizontal strain, which is characterized by a low magnitude. Poisson ratio standard uncertainties are comprised between 0.19 and 0.50, in the case of the optical method (see Section 4.2), while for the case of the contact method, this interval corresponds to 0.10 and 0.32 (see Section 4.3). In a global perspective, the mentioned dispersion of values has a higher magnitude than the measurement sample dispersion, between 0.03 and 0.09 (see Table 5).

This study showed that the suitability of the new approach proposed, based on non-invasive optical measurements applied to the destructive compressive mechanical testing of masonry specimens, is able to provide comparable results to conventional invasive measurements obtained using LVDT sensors. However, the scope of the validation process will need to be further studied, considering that the described mechanical tests were performed in a real case scenario, using a reduced dimension sample

of masonry specimens, each one characterized by a high variability in terms of the record strain spatial distribution, and different measurement points were defined for the optical and contact measurement methods. In this context, the development of reference materials and the use of advanced optical systems based on PIV (particle image velocimetry) [13–15] are recommended as future validation work.

Based on the analysis of the results, the increase of confidence in the studied compressive mechanical properties of masonry specimens should be focused on the sampling process, e.g., by increasing the number of local strain measurements in the specimen (thus reducing the average standard deviation related to the strain spatial variability) and also the number of specimens of a certain type (hollow or solid).

Author Contributions: L.F.L.M. and A.I.M. conceived, designed and performed the experiments and analyzed the data. Á.S.R. and P.C. validated the obtained results. L.F.L.M. and A.I.M. also wrote the paper, which was reviewed by Á.S.R. and M.d.R.V.; P.C., M.d.R.V. and J.G.F. contributed to the experiments by scientific supervision. All authors have read and agreed to the published version of the manuscript.

Funding: This research received the financial funding of LNEC—National Laboratory for Civil Engineering.

Acknowledgments: The authors are grateful to the Earthquake Engineering and Structural Dynamics Unit and the Structural Behaviour Unit of the LNEC’s Structures Department for gently providing the used testing equipment. The authors also acknowledge the technical support of the Electrotechnical and Mechanical Systems Unit of LNEC’s Scientific Instrumentation Centre, namely, in the production of the used synchronization signal generator, measurement referential and monitoring targets.

Conflicts of Interest: The authors declare no conflict of interest.

Appendix A

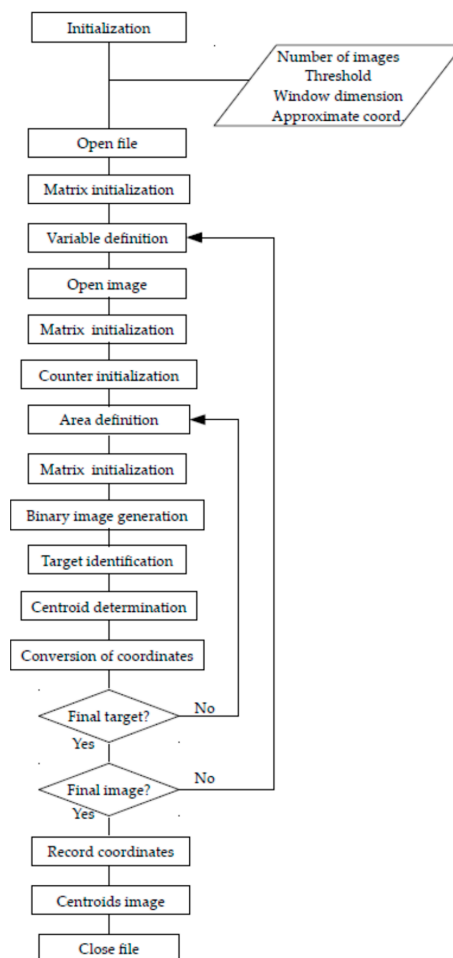


Figure A1. Digital image processing algorithm.

Appendix B

Table A1. Sample of calculated scale coefficients related to referential A.

Reference Targets Ids.	$D_{i,j}$ /mm	$d_{i,j}$ /pixel	$K_{i,j}$ /mm·pixel ⁻¹
1-2	89.985	478.5	0.188 0
1-3	179.717	954.6	0.188 3
1-4	201.027	1029.2	0.195 3
1-5	254.387	1274.7	0.199 6
1-6	200.962	995.6	0.201 8
1-7	180.049	903.9	0.199 2
1-8	90.286	459.4	0.196 5
2-3	89.733	476.2	0.188 4
2-4	126.970	630.6	0.201 3
2-5	200.892	985.6	0.203 8
2-6	179.483	883.0	0.203 3
2-7	201.105	1025.3	0.196 1
2-8	127.325	660.2	0.192 8
3-4	89.854	455.6	0.197 2
3-5	179.703	896.1	0.200 5
3-6	200.720	1025.1	0.195 8
3-7	254.303	1329.1	0.191 3
3-8	201.057	1062.2	0.189 3
4-5	89.849	440.6	0.203 9
4-6	126.899	646.1	0.196 4
4-7	201.065	1044.8	0.192 4
4-8	179.756	926.5	0.194 0
5-6	89.926	461.7	0.194 8
5-7	179.926	927.8	0.193 9
5-8	200.970	1009.6	0.199 1
6-7	90.001	466.3	0.193 0
6-8	126.847	622.3	0.203 8
7-8	89.763	444.6	0.201 9

Table A2. Sample of calculated scale coefficients related to referential B.

Reference Targets Ids.	$D_{i,j}$ /mm	$d_{i,j}$ /pixel	$K_{i,j}$ /mm·pixel ⁻¹
1-2	90.052	448.7	0.200 7
1-3	180.019	899.8	0.200 1
1-4	201.284	992.8	0.202 7
1-5	254.612	1247.3	0.204 1
1-6	201.066	968.9	0.207 5
1-7	179.915	862.8	0.208 5
1-8	89.938	433.6	0.207 4
2-3	89.967	451.2	0.199 4
2-4	127.367	618.4	0.205 9
2-5	201.382	971.9	0.207 2
2-6	179.824	852.4	0.211 0
2-7	201.198	963.8	0.208 8
2-8	127.150	612.3	0.207 6
3-4	90.224	437.4	0.206 3
3-5	180.235	868.6	0.207 5
3-6	201.081	968.3	0.207 7
3-7	254.448	1240.5	0.205 2
3-8	201.061	989.1	0.203 3
4-5	90.011	431.4	0.208 7
4-6	126.937	609.2	0.208 4
4-7	201.015	980.0	0.205 1
4-8	179.736	880.5	0.204 1
5-6	89.849	444.8	0.202 0
5-7	179.807	886.7	0.202 8
5-8	201.063	985.7	0.204 0
6-7	89.959	442.0	0.203 5
6-8	127.041	611.1	0.207 9
7-8	89.977	429.3	0.209 6

Appendix C

This appendix exemplifies the measurement uncertainty calculation for the compressive strength output quantity in the mechanical testing of masonry specimens, including the probabilistic formulation of the cross-section area and maximum load force measurements.

Based on the calibration certificate of the used universal testing machine, the compression force expanded measurement uncertainty, considering a 95% confidence interval, which corresponded to 0.53% of the force estimate value, in the measurement interval comprised between 300 and 3000 kN. This Gaussian dispersion value reflects both the measurement uncertainty component related to the applied calibration force and to the force measuring chain of the testing machine, namely, reproducibility, repeatability, interpolation, zero deviation, reversibility, and creep measurement uncertainty components. Table A3 shows the obtained maximum load force estimates and standard measurement uncertainties for several tested masonry specimens.

Table A3. Maximum load force measurements in tested masonry specimens.

Specimen Identification	Specimen Type	Estimate, F_{\max} /kN	Standard Uncertainty, $u(F_{\max})$ /kN
M0F3	Hollow	351.00	0.93
M0F7		375.32	0.99
M0F9		373.74	0.99
M0M9	Solid	929.1	2.5
M0M10		1292.6	3.4
M0M12		706.3	1.9

With respect to the cross-section area, its indirect determination is supported in linear measurements of the specimen's length and width, namely, three equally spaced measurements in its top surface and two additional measurements in the bottom surface, using a ruler tape with a resolution equal to 1 mm. Table A4 shows the obtained average values for the specimen's length and width and the corresponding standard measurement uncertainties, which combine the instrumental resolution (related to an uniform PDF with a semi-amplitude equal to 0.5 mm) with the average experimental standard deviation (obtained from the measurement samples with dimension equal to five). The presented cross-section area standard measurement uncertainties were obtained from the application of Equation (14).

Table A4. Cross-section area measurements in tested masonry specimens.

Specimen Identification	Specimen Type	Length, l /mm	Width, w /mm	Area, A /m ²
M0F3	Hollow	700.8 ± 0.7	244.0 ± 2.0	0.171 0 ± 0.001 4
M0F7		671.6 ± 0.9	246.0 ± 1.0	0.165 2 ± 0.000 7
M0F9		693.0 ± 3.0	246.0 ± 3.0	0.170 5 ± 0.002 2
M0M9	Solid	703.0 ± 1.3	247.6 ± 1.6	0.174 1 ± 0.001 2
M0M10		702.0 ± 1.1	245.0 ± 3.0	0.172 0 ± 0.002 1
M0M12		684 ± 10	246.2 ± 0.6	0.168 4 ± 0.002 5

Based on the information mentioned in the previous Tables A3 and A4, the compressive strength estimates and standard measurement uncertainties were determined for each tested masonry specimen using, respectively Equations (1) and (11). The obtained results are shown in Table A5.

Table A5. Compressive strength measurements in the tested masonry specimens.

Specimen Identification	Specimen Type	Estimate, σ /MPa	Standard Uncertainty, $u(\sigma)$ /MPa
M0F3	Hollow	2.053	0.018
M0F7		2.272	0.011
M0F9		2.194	0.028
M0M9	Solid	5.338	0.038
M0M10		7.515	0.094
M0M12		4.194	0.063

References

- Tomassetti, U.; Correia, A.A.; Graziotti, F.; Marques, A.I.; Mandirola, M.; Candeias, P.X. *Collapse Shaking Table Test on a URM Cavity Wall Building Representative of a Dutch Terraced House*; Eucentre Research Report; Eucentre: Pavia, Italy, 2017.
- Correia, A.A.; Marques, A.I.; Bernardo, V.; Grotoli, L.; Tomassetti, U.; Graziotti, F. *Shake Table Test up to Collapse on a Roof Substructure of a Dutch Terraced House*; Eucentre Research Report; Eucentre: Pavia, Italy, 2017.
- Kallioras, S.; Correia, A.A.; Marques, A.I.; Bernardo, V.; Candeias, P.X.; Graziotti, F. *LNEC-Build-3: An Incremental Shake-Table Test on a Dutch URM Detached House with Chimneys*; Eucentre Research Report EUC203/2018U; Eucentre: Pavia, Italy, 2018.
- Caporale, A.; Parisi, F.; Asprone, D.; Luciano, R.; Prota, A. Micromechanical analysis of adobe masonry as two-component composite: Influence of bond and loading schemes. *Compos. Struct.* **2014**, *112*, 254–263. [[CrossRef](#)]
- Greco, F.; Leonetti, L.; Luciano, R.; Nevone Blasi, P. An adaptive multiscale strategy for the damage analysis of masonry modeled as a composite material. *Compos. Struct.* **2016**, *153*, 972–988. [[CrossRef](#)]
- Wang, G.; Wu, Q.M.J. *Guide to Three Dimensional Structure and Motion Factorization*; Advances in Pattern Recognition; Springer: London, UK, 2011; pp. 29–32.
- Methods of Test for Masonry-Part 1: Determination of Compressive Strength*; EN 1052-1:1998; CEN—European Committee for Standardization: Brussels, Belgium, 1998.
- Marques, A.I.; Ferreira, J.G.; Candeias, P.X.; Veiga, M.R. Axial compression and bending tests on old masonry walls. In Proceedings of the 3rd International Conference on Protection of Historical Constructions, Lisbon, Portugal, 12–15 July 2017.
- Marques, A.I.; Candeias, P.X.; Ferreira, J.G.; Veiga, M.R. Caracterização de paredes resistentes de alvenaria antiga. In Proceedings of the Congress Euro-American REHABEND 2016 Patología de la Construcción, Tecnología de la Rehabilitación y Gestión del Patrimonio, Burgos, Spain, 24–27 May 2016.
- Methods of Test for Masonry. Determination of Flexural Strength*; EN 1052-2:1999; CEN—European Committee for Standardization: Brussels, Belgium, 1999.
- GUM. *Guide to the Expression of Uncertainty in Measurement*, 1st ed.; ISO—International Organization for Standardization (ISO): Genève, Switzerland, 1993.
- GUM-S1. Evaluation of measurement data. Supplement 1 to the Guide to the expression of Uncertainty in Measurement. In *Propagation of Distributions Using a Monte Carlo Method*, 1st ed.; JCGM—Joint Committee for Guides in Metrology: Genève, Switzerland, 2008.
- Corr, D.; Accardi, M.; Graham-Brady, L.; Shah, S. Digital image correlation analysis of interfacial debonding properties and fracture behavior in concrete. *Eng. Fract. Mech.* **2007**, *74*, 119–127. [[CrossRef](#)]
- Tekieli, M.; De Santis, S.; de Felice, G.; Kwiecień, A.; Roscini, F. Application of Digital Image Correlation to composite reinforcements testing. *Compos. Struct.* **2017**, *160*, 670–688. [[CrossRef](#)]
- Caggigi, C.; Sciuto, D.; Cuomo, M. Experimental study on effective bond length of basalt textile reinforced mortar strengthening system: Contributions of digital image correlation. *Measurement* **2018**, *129*, 119–127. [[CrossRef](#)]

